# Optimising the transformation and yield to ultimate strength ratio of Nb-Ti micro-alloyed low carbon line pipe steels through alloy and microstructural control

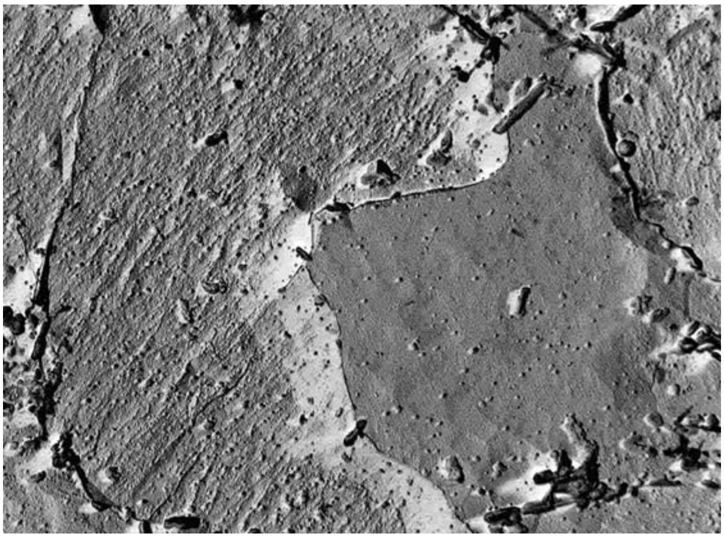

By Zhenghua Tang

Submitted in partial fulfilment of the requirements for the degree

Philosophiae Doctor (Metallurgical Engineering)

in the

Department of Materials Science and Metallurgical Engineering

Faculty of Engineering, Built Environment and Information Technology

University of Pretoria

Republic South Africa

22 May 2006

To my daughter Mingyi

谨此献给我的女儿唐铭艺

# Acknowledgments

Firstly, I would like to express my sincere gratitude and appreciation to Professor Waldo Stumpf* for his supervision, invaluable guidance and discussions and professor Chris Pistorius, Head of Department, and the University of Pretoria for the provision of facilities and financial support.

*Membership of national and international bodies:

- Fellow of the South African Academy of Engineering
- Past Chairman of the UN-International Atomic Energy Agency's Standing Advisory Group on Technical Assistance and Co-operation (SAGTAC) in Vienna for the years 2002 to 2005
- Past Member of an Expert Group of the UN-IAEA in 2004/2005 on the non-proliferation considerations of Multi-National Arrangements on Uranium enrichment and spent fuel reprocessing
- Past Honorary President of the South African Branch of the Institution of Nuclear Engineers

I would like to specially thank the following kind people:

Dr N.G. van den Bergh for technical support in shadowing replicas.

Professor G.T.van Rooyen for useful discussions and technical support in the tensile tests.

Mr CF van der Merwe for technical support in much of the work on transmission electron microscopy.

Mr Charl Smal for technical support in tensile tests and others.

Mr Johann Borman for his assistance before his untimely death.

I also wish to thank

Dr Kevin Banks for providing materials for the alloys and making many helpful suggestions.

Mr Francois Verdoorn for training on the Gleeble and Dilatometer.

Mrs Havenga Sarah for her assistance in administrative matters.

Mr Charles Siyasiya for his assistance in editing my English.

I would like also to thank others who gave me assistance.

The provision of financial support from Mittal Steel SA and the NRF through the THRIP program is also greatly appreciated.

Finally, I would like to also specially thank my wife and my daughter Mingyi for they gave me a wonderful and memorable life of four years in far SA and, for their assistance and encouragement.

致谢

首先,我要衷心的感谢我的导师, 南非工程院院士, 2002-2005 维也纳联合国原子能机构技术支持与协助顾问团主席, 2004/2005 联合国多国铀废料回收专家组成员,核工程协会南非分会前名誉主席, 比勒陀利亚大学教授, Stumpf 先生对我的精心指导! 和比勒陀利亚大学材料科学与冶金工程系主任 Pistorius 教授以及大学所给予的设备和资金方面的支持!

特别感谢如下的南非友好人士:

N.G. van der Berg 博士在电镜投影复型方面的技术支持;

G.T.van Rooyen 教授的有益讨论和特殊拉伸试验方面的帮助;

CF van der Merwe 先生在透射电镜实验方面提供的方便;

Charl Smal 先生在拉伸试验和其他方面的帮助;

Johann Borman 先生生前非常友好的帮助;

还要感谢

Kevin Banks 博士提供了实验所需的材料及一些有益的建议;

Verdoorn Francois 先生在 Gleeble 和 Dilatometer 的培训;

Havenga Sarah 女士在行政事务方面的帮助;

Mr Charles Siyasiya 在校正英语方面的帮助;

以及其他给予帮助的人士;

还要感谢南非 Mittal 钢公司及 THRIP 项目所给予的资金支持;

此外,我特别要感谢我的妻子和女儿陪伴我在遥远的南非度过了令我终身难忘的非常快乐的四年海外生活，同时她们也给了我无数的帮助和鼓励。

# Optimising the transformation and yield to ultimate strength ratio of Nb-Ti micro-alloyed low carbon line pipe steels through alloy and microstructural control

by Zhenghua Tang (唐正华)

Supervisor: Professor Waldo Stumpf

Department: Materials Science and Metallurgical Engineering

University: University of Pretoria

Degree: Philosophiae Doctor

## Abstract

Thinner walled (about 6 mm thickness) line pipe steels for smaller diameter pipelines tend to have a relatively high ratio of yield strength to ultimate tensile strength (YS/UTS) of 0.93 or higher. This study focused on the effect of the microstructures, prior deformation in the austenite, cooling rate, coiling simulation and the additions of some micro-alloying elements on the YS/UTS ratio of a currently produced Nb-Ti and some experimental Nb-Ti-Mo line pipe steels. The experimental research included the design of the chemical compositions for five experimental alloys, simulation of the controlled hot rolling process, the determination of the strain-free as well as the strain affected continuous cooling transformation (CCT) diagrams, phase identification and quantitative assessment of the microstructures by optical microscopy, scanning electron microscopy (SEM) and transmission electron microscopy (TEM), the latter especially on shadowed carbon extraction replicas and, tensile tests etc.

This study indicated that the transformed microstructures of the alloys were a mixture of acicular ferrite plus polygonal ferrite and the volume fraction of acicular ferrite varied from 46.3 to 55.4%. Molybdenum additions did not markedly affect the

formation of acicular ferrite after hot rolling and rapid cooling. The microstructural details of the acicular ferrite were successfully revealed by TEM on shadowed extraction replicas. This technique was useful to distinguish the acicular ferrite from the polygonal ferrite through a more smooth surface relief after etching in 2% Nital of the little etched polygonal ferrite whereas the deeper etched acicular ferrite showed parallel sets of internal striations. This made it possible to measure the volume fraction of acicular ferrite in the mixed microstructures of acicular ferrite and polygonal ferrite.

The continuous cooling transformation behaviors of two alloys with no molybdenum and with 0.22% Mo were constructed with no prior deformation as well as with prior deformation of the austenite. Molybdenum additions shifted the strain-free CCT diagram towards longer times and expanded the region in which acicular ferrite formed from a cooling rate range of 0.3 to 5 ºC$s^{-1}$ (Mo-free) to 0.1 to 15 ºC$s^{-1}$ (with 0.22% Mo). However, its effect was significantly overshadowed by prior deformation in the austenite. The strain affected CCT diagrams for both alloys appear to be similar. The prior deformation had a stronger effect on the CCT diagram than molybdenum additions and promoted acicular ferrite formation, whereas it suppressed the formation of bainite. The prior deformation had two effects in acicular ferrite formation: it promoted nucleation and suppressed its growth and, therefore, resulted in a finer overall grain size.

The effect on the YS/UTS ratio at various cooling rates ranging from 1 to 34, 51, 54 or 60 ºC$s^{-1}$ was investigated in three cases: (i) without prior deformation and coiling simulation, (ii) with no prior deformation but with coiling simulation at 575 and 600 ºC and, (iii) with prior deformation of 33% reduction in the austenite below the $T_{nr}$ followed by coiling simulation at 575 ºC for 1 hour. It was determined that the YS/UTS ratio was a function of the microstructure and cooling rate in the case (treatment (i)) without any coiling simulation and prior deformation. The coarse bainite or acicular ferrite, which was formed at high cooling rates, raised the YS/UTS ratio under conditions of no deformation prior to the transformation. The yield strength and ultimate tensile strength also increased with an increase in cooling rate.

With coiling conditions (treatment (ii)), the ratio was not sensitive to the cooling rate or the microstructure for the reference Mo-free alloy #6 because the coiling allows recovery of dislocations, thereby decreasing the difference in dislocation density that had arisen between a low and a high cooling rate. The YS/UTS ratio ranged from 0.75 to 0.8 after a simulated coiling at 575 ºC and from 0.76 to 0.78 after a coiling simulation at 600 ºC.

Prior deformation (treatment (iii)) in the austenite raised the ratio from 0.81 to 0.86. However, the YS/UTS ratio was not sensitive to cooling rate after coiling at 575 ºC for 1 hour in the cases with and without prior deformation in the austenite. Deformation with a 33% reduction below the $T_{nr}$ prior to the transformation increased the yield strength more than the ultimate tensile strength, leading to a high YS/UTS ratio that ranged from 0.81 to 0.86. The prior deformation, therefore, had a stronger effect on the YS/UTS ratio than the microstructure.

**Key words:**
line pipe steel, acicular ferrite, microstructure, ratio of yield strength to ultimate tensile strength,, Nb-Ti micro alloyed steel, controlled hot rolling process, CCT diagram, non-recrystallisation temperature, nucleation of acicular ferrite

**Table of Contents**

Acknowledgments……………………………………………………………………ii
Abstract………………………………………………………………………………v

CHAPTER 1 INTRODUCTION……………………………………………………1
1.1 Strengthening mechanisms in line pipe steels……………………………………..1
1.2 Chemical composition of line pipe steels…………………………………….…1
1.3 Steel making of line pipe steel…………………………………………………2
1.4 The controlled rolling of strip steel……………………………………………..3
1.4.1 Rolling schedule………………………………………………………………3
1.4.1.1 Reheating…………………………………………………………………3
1.4.1.2 Rough rolling……………………………………………………………...3
1.4.1.3 Finish rolling……………………………………………………………...4
1.4.1.4 Heavy reduction…………………………………………………………..4
1.4.2 Cooling rate……………………………………………………………………...5
1.4.3 Coiling temperature……………………………………………………………...5
1.5 Pipe forming and welding process ………………………………………………5

CHAPTER 2 MICRO-ALLOYING ELEMENTS AND THEIR EFFECT ON PRECIPITATION……………………………………………………7
2.1 Vanadium………………………………………………………………………..7
2.2 Niobium…………………………………………………………………………7
2.3 Titanium……………………………………………………………………….…...9
2.4 Molybdenum……………………………………………………………….……..10
2.5 Carbon…………………………………………………………………….…11
2.6 Manganese……………………………………………………………………..11
2.7 Copper, Chromium and Nickel…………………………………………………...12

CHAPTER 3 THE CONTROLLED ROLLING PROCESS OF LINE PIPE STEELS ………………………………………………………………….…...13
3.1 Three stages of deformation for controlled rolling process……….……………...13
3.1.1 Deformation in the austenite recrystallisation region…………………….……14
3.1.2 Deformation in the non-recrystallisation region………………………….……..14
3.1.3 Deformation in the (α+γ) two-phase region…………………………………15

3.2 Reheating temperature and undissolved particles……………………………..16
3.3 Rough rolling…………………………………………………………………….18
3.4 Finish rolling……………………………………………………………………..19
3.5 Heavy reductions…………………………………………………………………21
3.6 Strip thickness…………………………………………………………………….22
3.7 Cooling rate after finish rolling…………………………………………………..23
3.8 Finish temperature of accelerated cooling……………………………………..25
3.9 Coiling temperature……………………………………………………………….27
3.10 Non-recrystallisation temperature ($T_{nr}$)………………………………………28
3.10.1 Effect of alloying elements……………………………………………………28
3.10.2 Effect of the controlled rolling process……………………………………..29

CHAPTER 4 MICROSTRUCTURE AND MECHANICAL PROPERTIES………..32
4.1 Acicular ferrite…………………………………………………………………….32
4.1.1 Nucleation and growth of acicular ferrite……………………………………32
4.1.2 Two types of acicular ferrites: upper and lower acicular ferrite……………..33
4.1.3 Effect of the hot rolling process on acicular ferrite formation………………35
4.2 Acicular ferrite and bainite……………………………………………………….35
4.3 Mechanical properties of line pipe steel…………………………………………36
4.3.1 The ratio of yield strength to ultimate tensile strength (YS/UTS)…………..36
4.3.2 Toughness………………………………………………………………………38
4.3.3 U-O pipe forming and the Bauschinger effect………………………………38

CHAPTER 5 BACKGROUND OF CURRENT SOUTH AFRICA LINE PIPE PRODUCTION……………………………………………………………………..42
5.1 Line pipe steel composition of Mittal Steel (South Africa)………………………42
5.2 Parameters of the hot rolling process at Mittal Steel (SA)………………………43
5.3 Typical microstructures and existing developments within Mittal Steel for line pipe steel……………………………………………………………………………44
5.4 The hypothesis for this study…………………………………………………….45
5.4.1 Design of chemical compositions of the investigated alloys………………..45
5.4.2 Design of the controlled hot rolling process…………………………………...46

CHAPTER 6 EXPERIMENTAL PROCEDURES……………………………………...49
6.1 Alloy design……………………………………………………………………49
6.2 The melting of the experimental alloys………………………………………..50
6.3 The effect of reheating temperature and soaking time on the austenite grain size ……………………………………………………………………………………51
6.4 Measuring the presence and composition of undissolved particles……………...53
6.5 Non-recrystallisation temperature ($T_{nr}$)………………………………………54
6.5.1 Testing schedule for the determination of the $T_{nr}$………………………………55
6.5.2 The determination of the non-recrystallisation ($T_{nr}$)…………………………57
6.6 CCT diagram……………………………………………………………………59
6.6.1 The $A_{c1}$ and $A_{c3}$ test…………………………………………………………59
6.6.2 CCT diagram without prior deformation………………………………………60
6.6.3 Strain affected CCT diagram……………………………………………………61
6.7 The thermo-mechanical process…………………………………………………63
6.7.1 Cooling unit……………………………………………………………………63
6.7.2 Hot rolling process of the laboratory ingots……………………………………64
6.7.2.1 Reheating before laboratory hot rolling………………………………………64
6.7.2.2 Rough rolling of the laboratory hot rolling…………………………………64
6.7.2.3 Finish rolling of the laboratory hot rolling…………………………………65
6.7.2.4 Cooling rate after laboratory finish rolling…………………………………65
6.7.2.5 Simulation of coiling after laboratory hot rolling…………………………..65
6.7.2.6 Hot-rolling process curve……………………………………………………..66
6.8 The identification of acicular ferrite…………………………………………..66
6.8.1 Observation with optical microscopy and by SEM……………………………67
6.8.2 Observation of replicas by TEM……………………………………...……..68
6.8.2.1 Preparing replicas without shadowing………………………………………68
6.8.2.2 Preparing shadowed carbon extraction replicas ……………………………68
6.8.3 Thin foil TEM samples…………………………………...…………….68
6.9 Test of subsize samples on the Gleeble with various cooling rates, coiling temperatures and prior deformation……………………………………..……..69
6.9.1 Hot rolling plates for Gleeble samples………………………………….……..69
6.9.2 Tests on the Gleeble…………………………………………………….……..70
6.9.3 Tensile tests……………………………………………………………….…...72
6.10 Test of mechanical properties on the as-hot rolled alloys……………………..…..73

CHAPTER 7 RESULTS……………………………………………………………..74

7.1 The effect of the austenitisation temperature and holding time on the presence of undissolved particles in the V-Nb-Ti-containing alloys………………………....74

7.2 Austenite grain size and reheating temperature…………………………………..85

7.3 The non-recrystallisation temperature ($T_{nr}$) and deformation parameters………..88

7.3.1 The $T_{nr}$ and pass strain…………………………………………………………89

7.3.2 The $T_{nr}$ and inter-pass time……………………………………………….……93

7.3.3 The $T_{nr}$ and pass strain rate……………………………………………….……99

7.4 Continuous cooling transformation (CCT diagrams) under strain-free conditions ……………………………………………………………………………..104

7.4.1 CCT diagram for alloy #6 without molybdenum and without prior deformation ……………………………………………………………………..……..104

7.4.2 CCT diagram for alloy #5 with 0.22% molybdenum and without prior deformation………………………………………………………….…..109

7.5 Strain enhanced continuous cooling transformation (CCT diagram) under deformed conditions…………………………………………………...…113

7.5.1 Strain affected CCT diagram of the Mo-free alloy #6……………………..…..114

7.5.2 Strain affected CCT diagram of alloy #5 (with 0.22% Mo)……………..……..118

7.6 The results of the laboratory hot rolling process on the YS/UTS ratio…………124

7.7 Volume fraction of acicular ferrite ……………………………………………..125

7.8 Mechanical properties…………………………………………………………..125

7.8.1 Results of experimental alloys…………………………………………………125

7.8.2 Results of mechanical properties for different cooling rates, coiling temperatures and deformation values……………………………………126

7.8.2.1 Effect of cooling rate with no coiling and no prior deformation………..126

7.8.2.2 Effect of cooling rate with coiling but without deformation……………128

7.8.2.3 Effect of cooling rate and 575 ºC coiling with a 33% prior reduction below the $T_{nr}$…………………………………………………………………129

7.9 Transformed microstructures of the alloys……………………………………..129

7.9.1 Optical micrographs…………………………………………………………..129

7.9.2 Microstructures examined by SEM………………………………………..…..131

7.9.3 TEM studies of acicular ferrite on carbon replicas………………………...135

CHAPTER 8 STUDIES OF ACICULAR FERRITE BY THIN FOIL TEM..…….140
8.1 Acicular ferrite morphology in experimental alloys……………………………140
8.1.1 Acicular ferrite and polygonal ferrite in alloy #6 (Mo-free)………………...141
8.1.2 Acicular ferrite and polygonal ferrite in alloy #1……………………………145
8.1.3 Acicular ferrite in alloys #2 to #5……………………………………………148
8.2 Two types of acicular ferrite……………………………………………………….156
8.2.1 Structure with parallel laths……………………………………………………156
8.2.2 Structure with interwoven laths……………………………………………...…..159
8.3 Nucleation of acicular ferrite………………………………………………………162
8.3.1 Nucleation on non-metallic inclusions……………………………………….162
8.3.2 Type of non-metallic inclusion as nucleants……………………………...….168
8.3.3 Nucleation mechanisms of acicular ferrite………………………………….168

CHAPTER 9 DISCUSSION…………………………………………………………174
9.1 Effect of molybdenum additions on the continuous cooling transformations.…174
9.1.1 Effect of molybdenum on polygonal ferrite formation……………………...174
9.1.2 Effect of molybdenum on acicular ferrite formation……………………..….175
9.2 Effect of deformation in austenite on acicular ferrite formation……………..….176
9.3 Ratio of yield strength to ultimate tensile strength and its effect……………......179
9.3.1 The effect of cooling rate……………………………………………………179
9.3.2 The effect of coiling temperature……………………………………………183
9.3.3 The effect of prior deformation in the austenite and coiling simulation…….187
9.3.4 The effect of acicular ferrite on the ratio of yield strength to ultimate tensile strength……………………………………………………………………...190

CHAPTER 10 CONCLUSIONS…………………………………………………..…..192

CHAPTER 11 RECOMMENDATIONS FOR FUTURE WORK……………………..195

References…………………………………………………………………………...…196

Appendix……………………………………………………………………………….205

**List of figures:**

Figure 3.1 Schematic illustration of the three stages of the controlled rolling process[11].

Figure3.2 Metallurgical mechanisms during thermo mechanical hot rolling[8].

Figure 3.3 Correlation between the increase in yield strength ΔYS and the content of soluble Nb[24] (0.075% C, 043% Si, 1.58% Mn, 0.013% P, 0.005% S, 0.51% Ni, 0.021% Al and 0.106% Nb, and 0.077% C, 0.36% Si, 1.56% Mn, 0.017% P, 0.005%S, 0.47% Ni, 0.020% Al and 0.130% Nb).

Figure 3.4 Comparison between the calculated and measured quantities of micro-alloying elements as precipitates[37].

Figure 3.5 Change in austenite grain size during reheating process[39].

Figure 3.6 Influence of rolling conditions on the mechanical properties of plate and strip of different thicknesses[24].

Figure 3.7 Influence of rolling conditions on the average ferrite grain size[24].

Figure 3.8 Improvement in yield strength and Charpy ductile to brittle transition temperature[10].

Figure 3.9 Plot of the volume fraction of M/A constituents versus the degree of prior deformation[13].

Figure 3.10 Strip and pipe properties for various X80 pipe sizes)[6]. (Steel G: 0.075% C, 1.59% Mn, 0.31% Si, 0.057% Nb, 0.22% Mo, 0.013% Ti and 0.006% N; Steel N: 0.070% C,1.53% Mn, 0.19% Si, 0.045 Nb,0.20% Mo, 0.012% Ti and 0.0045% N.

Figure 3.11 Schematic representation of the cooling pattern on the run-out table of a Hot Strip Mill[2].

Figure 3.12 Influence of reduction and cooling rate on the ferrite grain diameter[10].

Figure 3.13 Effect of finish temperature of accelerated cooling on the average ferrite grain diameter[39].

Figure 3.14 Comparison of mechanical properties between the observed and the calculated strengths of micro-alloyed steels[39].

Figure 3.15 Effect of coiling temperature on the YS of hot rolled strip for various types of alloys[2].

Figure 4.1 Schematic stress-strain curves for the outer (top) and inner (bottom) material during the U-O pipe forming process, with (left) at 180º and (right) at 30º from the welding line[93].

Figure 4.2 The change of the Bauschinger effect factor with carbon and manganese content[94].

Figure 4.3 The Bauschinger effect in micro-alloyed steel. The upper two curves are for steels with 0.2% C, 0.4% Mn, unalloyed or alloyed respectively with Al, V or Nb. The lower two curves are for low-pearlite steels with less than 0.1% C, 2% Mn, and alloyed with Mo, Nb and Ti[94].

Figure 5.1 The optical microstructure of cast #521031, Mittal Steel line pipe

Figure 6.1 Schematic of the modified McQuaid-Ehn carburising process of the samples directly after reheating.

Figure 6.2 Schematic schedule employed in the multi-pass compression tests for the $T_{nr}$.

Figure 6.3 The curves of flow stress versus strain in a multi-pass compression test on alloy #6.

Figure 6.4 Determining $T_{nr}$ from the mean flow stress in MPa versus the inverse pass temperature in K, during a multi-pass compression test on alloy #6.

Figure 6.5 Schematic dilation as a function of testing temperature[126].

Figure 6.6 Schematic determination of the $A_{c1}$ and $A_{c3}$ temperatures on the heating curve[126].

Figure 6.7 Dilatometer chamber

Figure 6.8 Schematic schedule of the test for the CCT diagram on the THETA Dilatometer.

Figure 6.9 Chamber of the Gleeble 1500$^D$ DSI

Figure 6.10 Schematic schedule of the test for the strain affected CCT diagrams on the Gleeble.

Figure 6.11 Experimental arrangement of the cooling unit for controlled cooling: (a) overall view, (b) controller for mixing of gas and water, (c) valves for the nozzles and, (d) cooling spray in the chamber from the spraying jets.

Figure 6.12 Schematic schedule of the hot rolling process on the experimental alloys.

Figure 6.13 Preliminary samples on the Gleeble of (a) type A and (b) type B

Figure 6.14 Graph of the heating and cooling process on the Gleeble for samples #A124 (the Mo-free alloy #6) and sample #AF3F (the 0.09% Mo alloy #3).

Figure 6.15 Graphs of the heating and cooling cycles in the Gleeble on the Mo-free alloy #6 for samples (a) #A113 and (b) #B113.

Figure 6.16 Graph of heating, cooling and deformation process in the Gleeble for sample #TEN06 (the Mo-free alloy #6).

Figure 6.17 Tensile test samples of (a) type A and (b) type B. T is original thickness of the plates and 6 mm for the as-rolled alloy and the Gleeble samples, respectively.

Figure 7.1 Extraction replicas without shadowing with undissolved particles for alloy #6 after reheating at 1200 ºC for 15 min. (Most of the darker spots are not particles but are etching debris on the replicas).

Figure 7.2 Extraction replicas with Au-Pd shadowing for alloy #6 after reheating at 1225 ºC for 120 min.

Figure 7.3 TEM micrograph of particles on the shadowed replicas of alloy #6 reheated at 1150 ºC for (a) 15 min, (b) 60 min and, (c) 120 min.

Figure 7.4 TEM micrograph of particles on the shadowed replicas of alloy #6 reheated at 1200 ºC for (a) 15 min, (b) 60 min and, (c) 120 min.

Figure 7.5 TEM micrograph of particles on the shadowed replicas of alloy #6 reheated at 1225 ºC for (a) 15 min, (b) 60 min and, (c) 120 min.

Figure 7.6 TEM micrograph of particles on the shadowed replicas of alloy #6 reheated at 1250 ºC for (a) 15 min, (b) 60 min and, (c) 120 min.

Figure 7.7 TEM-EDS results of undissolved particles of alloy #6 after the treatments of (a) as-hot rolled, (b) as-hot rolled, (c) 1150 ºC for 120 min and, (d) 1200 ºC for 15 min.

Figure 7.8 The effect of reheating temperature and time on the volume fraction of undissolved particles for alloy #6.

Figure. 7.9 Pro-eutectoid cementite decorates the original austenite grain boundaries in alloy #6 for soaking times of 60 min at different austenitisation temperatures.

Figure. 7.10 The relationship between the austenitisation temperature and the austenite grain size for alloy #6. The broken line is from published data[39].

Figure. 7.11 The weak effect of soaking time on the austenite grain size for alloy #6.

Figure 7.12 Stress-strain curves of multi-pass compression tests of alloy #6 at the same strain rate of 1 $s^{-1}$, inter-pass time of 8 seconds and different pass strains.

Figure 7.13 Determination of the $T_{nr}$ on the mean flow stress versus inverse temperature curves of alloy #6, all deformed at the same strain rate of 1 $s^{-1}$ and an inter-pass time of 8 seconds but at different pass strains.

Figure 7.14 The relationship between pass strain (ε) and the non-recrystallisation temperature for alloy #6. Strain rate $\dot{\varepsilon}$=1.0 $s^{-1}$, inter-pass time $t_{ip}$=8 s.

Figure 7.15 Stress-strain curves of multi-pass compression tests on alloy #6 at a c onstant pass strain of 0.20, a constant strain rate of 1 $s^{-1}$ and a series of inter-pass times ranging from 4 to 50 seconds.

Figure 7.16 The mean flow stress versus inverse temperature curve of alloy #6 during multi-pass compression testing at a constant pass strain of 0.20 and a constant strain rate of 1 $s^{-1}$ but with a variation of the inter-pass times between 4 and 50 seconds.

Figure 7.17 The $T_{nr}$ as a function of inter-pass time ($t_{ip}$) for alloy #6. Strain rate $\dot{\varepsilon}$ =1.0 $s^{-1}$, pass strain $\varepsilon$ = 0.2.

Figure 7.18 Stress-strain curves of compression deformation tests of alloy #6 at a constant pass strain of 0.20 and inter-pass time of 8 s but with a series of strain rates from 0.1 to 2.22 $s^{-1}$.

Figure 7.19 The mean flow stress versus inverse test temperature of alloy #6 at a constant pass strain of 0.20 and inter-pass time of 8 s but at a series of strain rates from 0.1 to 2.22 $s^{-1}$.

Figure.7.20 Strain rate ( $\dot{\varepsilon}$ ) versus the non-recrystallisation temperature for alloy #6. pass strain $\varepsilon$ = 0.2, inter-pass time $t_{ip}$=8 s.

Figure 7.21 The optical micrographs (etched in 2% Nital) of the Mo-free alloy #6 and with no prior deformation after continuous cooling. PF-polygonal ferrite, P-pearlite and AF-acicular ferrite microstructure.

Figure 7.22 The CCT diagram of the Mo-free alloy #6 and no prior deformation. PF-polygonal ferrite, P-pearlite, AF-acicular ferrite microstriucture and B-bainite.

Figure 7.23 The optical micrographs (etched in 2% Nital) for alloy #5 (with 0.22% Mo) and with no prior deformation after continuous cooling. PF-polygonal ferrite, P-pearlite and AF-acicular ferrite microstructure.

Figure 7.24 The CCT diagram of alloy #5 (with 0.22% Mo) and with no prior deformation. PF-polygonal ferrite, P-pearlite, AF-acicular ferrite microstructure and B-bainite.

Figure 7.25 The optical micrographs (etched in 2% Nital) of the Mo-free alloy #6 after compression testing with a single pass strain of 0.6 at 860 ºC (which is below the $T_{nr}$), a strain rate of 0.5 $s^{-1}$ and cooling down to room temperature at different cooling rates. PF-polygonal ferrite, P-pearlite and AF-acicular ferrite microstructure.

Figure 7.26 The strain affected CCT diagram of the Mo-free alloy #6 after a single pass compression strain of 0.6 at 860 ºC with a strain rate of 0.5 $s^{-1}$. PF-polygonal ferrite, P-pearlite and AF-acicular ferrite microstructure.

Figure 7.27 The optical micrographs (etched in 2% Nital) of alloy #5 (with 0.22% Mo) after a single pass compression of 0.6 strain at 860 ºC and at a strain rate of 0.5 $s^{-1}$ and then cooling at different rates.

Figure 7.28 The strain affected CCT diagram of alloy #5 (with 0.22% Mo) after a single pass compression of 0.6 strain at 860 ºC at a strain rate of 0.5 $s^{-1}$. PF-polygonal ferrite, P-pearlite and AF-acicular ferrite microstructure.

Figure 7.29 The optical microstructure, etched in a 2% Nital solution for 5 seconds, after a rapid cooling rate of 47 $^{o}Cs^{-1}$ for the experimental alloys (a) #1, (b) #2, (c) #3, (d) #4, (e) #5 and, (f) the reference Mo-free alloy #6 cooled at a rate of 39 $^{o}Cs^{-1}$.

Figure 7.30 The SEM micrographs after a rapid cooling rate of 47 $^{o}Cs^{-1}$(etched in 2% Nital for 5 seconds) for the experimental alloys (a) #1, (c) #2, (c) #3, (d) #4, (e) #5 and, (f) the reference alloy #6 cooled at a rat of 39 $^{o}Cs^{-1}$.

Figure 7.31 The micrographs in the as-rolled condition by high resolution SEM after a rapid cooling rate of 47 $^{o}Cs^{-1}$(etched in 2% Nital for 5 seconds) for the experimental alloys (a) #1, (c) #2, (c) #3, (d) #4 and, (e) #5.

Figure 7.32 The high resolution SEM micrographs in the as-rolled condition after a rapid cooling rate of 47 $^{o}Cs^{-1}$ for the experimental alloy #1 etched in 2% Nital for (a) 10seconds, (c) 15 seconds, (c) 30 seconds, (d) 60 seconds and, (e) 120 seconds.

Figure 7.33 TEM micrographs of carbon extraction replicas without shadowing for the reference alloy #6 after hot rolling and rapid cooling at a rate of 39 $^{o}Cs^{-1}$.

Figure 7.34 The TEM micrograph from a shadowed replica of the Mo-free alloy #6 after hot rolling and rapid cooling at a rate of 39 $^{o}Cs^{-1}$. (AF-acicular ferrite, PF-polygonal ferrite and, GB-grain boundary).

Figure 7.35 TEM micrographs from shadowed replicas of the as-hot rolled and rapidly cooled (at a rate of 47 $^{o}Cs^{-1}$) experimental alloys (a) #1, (b) #2, (c) #3, (d) #4 and, (e) #5 (AF-acicular ferrite, PF- polygonal ferrite and, GB-grain boundary).

Figure 8.1 Thin foil TEM micrographs of alloy #6 (Mo-free) after a rapid cooling rate of 39 °$Cs^{-1}$ after hot rolling, (a) polygonal ferrite + laths, (b) polygonal ferrite with dislocations and, (c),(d) laths with dislocations. PF-polygonal ferrite, AF-acicular ferrite, A and B-dislocations in polygonal ferrite and an acicular ferrite , respectively.

Figure 8.2 Dislocations within the polygonal ferrite in thin foil of the Mo-free alloy #6. The area M shows a high density of dislocations possibly being emitted from the moving PF interface while the central regions L of the PF have less dislocations.

Figure 8.3 Polygonal ferrite in a TEM thin foil micrograph from the experimental alloy #1 after a rapid cooling rate of 47 ºCs$^{-1}$ after the hot rolling process.

Figure 8.4 TEM thin foil micrograph with laths from alloy #1 after a rapid cooling rate of 47 ºCs$^{-1}$ after the hot rolling process.

Figure 8.5 TEM thin foil micrograph of the lath plus PF structure in alloy #1 after a rapid cooling rate of 47 ºCs$^{-1}$ after the hot rolling process.

Figure 8.6 Thin foil TEM micrographs of the lath structure in alloy #2 after a rapid cooling rate of 47 ºCs$^{-1}$ after the rolling process.

Figure 8.7 Thin foil TEM composite micrographs of parallel laths of an acicular ferrite in alloy #2 after a rapid cooling rate of 47 ºCs$^{-1}$ after the hot rolling process.

Figure 8.8 Polygonal ferrite (with a few isolated laths) in alloy #3 with a rapid cooling rate of 47 ºCs$^{-1}$ after the hot rolling process.

Figure 8.9 The parallel lath morphology in alloy #3 after a rapid cooling rate of 47 ºCs$^{-1}$ after the hot rolling process.

Figure 8.10 Thin foil TEM micrographs of a mixture of polygonal ferrite and an acicular ferrite in alloy #3 after a rapid cooling rate of 47 ºCs$^{-1}$ after the hot rolling process.

Figure 8.11 Thin foil TEM composite micrographs of the acicular ferrite in alloy #4 after a rapid cooling rate of 47 ºCs$^{-1}$ after the hot rolling process.

Figure 8.12 Thin foil TEM micrographs from alloy #5 with 0.22% Mo (a) polygonal ferrite, (b) and (c) acicular ferrite with interwoven laths.

Figure 8.13 Parallel lath morphology in a colony in alloy #3 after rapid cooling at a rate of 47 ºCs$^{-1}$ after the hot rolling process.

Figure 8.14 Interwoven arrangement between lath colonies in alloy #4 after a fast cooling rate of 47 ºCs$^{-1}$ after the hot rolling process.

Figure 8.15 Interwoven laths micrographs in alloy #3 after fast cooling of 47 ºCs$^{-1}$ after hot rolling process.

Figure 8.16 Acicular ferrite morphology in alloy #5 after fast cooling of 47ºCs$^{-1}$ after the hot rolling process.

Figure 8.17 (a) TEM image of acicular ferrite and a large non-metallic inclusion in alloy #5 after a rapid cooling rate of 47 ºCs$^{-1}$ after the hot rolling, (b) EDS analysis on the inclusion in this figure (a).

Figure 8.18 Laths nucleated on non-metallic inclusions (a) in alloy #1 after a rapid cooling rate of 47 ºCs$^{-1}$ after the hot rolling, (b) in alloy #3 after a rapid cooling rate of 40 ºCs$^{-1}$ from 980 ºC down to room temperature without deformation, (c) EDS analysis on the inclusion in this figure (a), (d) and (e) EDS analysis on the inclusions A and B in this figure (b), respectively.

Figure 8.19 (a) Nucleation of interwoven laths of acicular ferrite in sample #AF3F of alloy #3 after a cooling rate of 20 ºCs$^{-1}$ from 980 ºC down to room temperature without deformation, (b) EDS analysis of red peak was from on the inclusion indicated by an arrow in this figure (a), while blue peak was from the matrix steel.

Figure 8.20 (a) Non-metallic inclusion and acicular ferrite in alloy #3 after a rapid cooling rate of 47 ºCs$^{-1}$ after the hot rolling, (b) EDS analysis on the inclusion indicated by an arrow in this figure (a).

Figure 9.1 The yield strength of the reference Mo-free alloy #6 as a function of the cooling rate from 980 ºC with no prior deformation before the transformation and with no coiling simulation.

Figure 9.2 The ultimate tensile strength of the reference alloy #6 as a function of cooling rate from 980 ºC with no prior deformation before the transformation and with no coiling simulation.

Figure 9.3 The YS/UTS ratio of the reference alloy #6 as a function of cooling rate from 980 ºC with no prior deformation before the transformation and with no coiling simulation. PF-polygonal ferrite, AF-acicular ferrite and P-pearlite.

Figure 9.4 The yield strength of alloy #3 as a function of cooling rate from 980 ºC under conditions of no prior deformation to the transformation and no coiling simulation.

Figure 9.5 The ultimate tensile strength of alloy #3 as a function of cooling rate from 980 ºC under conditions of no prior deformation to the transformation and no coiling simulation.

Figure 9.6 The YS/UTS of alloy #3 as a function of cooling rate from 980 ºC underconditions of no prior deformation to the transformation and no coiling simulation.PF-polygonal ferrite, AF-acicular ferrite, B-bainite and P-pearlite

Figure 9.7 The yield strength of alloy #6 as a function of the cooling rate from 980 ºC to 600 ºC under conditions of no prior deformation to the transformation but with a coiling simulation at 600 ºC for 1 hour.

Figure 9.8 The ultimate tensile strength of alloy #6 as a function of cooling rate from 980 ºC to 600 ºC under conditions of no prior deformation to the transformation but with a coiling simulation at 600 ºC for 1 hour.

Figure 9.9 The YS/UTS ratio of alloy #6 as a function of the cooling from 980 ºC to 600 ºC under conditions of no prior deformation to the transformation but with a coiling simulation at 600ºC for 1 hour. PF-polygonal ferrite, AF-acicular ferrite, B-bainite and P-pearlite.

Figure 9.10 The yield strength of alloy #6 as a function of the cooling rate from 980 ºC to 575 ºC under conditions of no prior deformation to the transformation but with a coiling simulation at 575 ºC for 1 hour.

Figure 9.11 The ultimate tensile strength of alloy #6 as a function of the cooling rate from 980 ºC to 575 ºC under conditions of no prior deformation to the transformation but with a coiling simulation at 575 ºC for 1 hour.

Figure 9.12 The YS/UTS ratio alloy #6 as a function of the cooling rate from 980 ºC to 575 ºC under conditions of no prior deformation to the transformation but with a coiling simulation at 575 ºC for 1 hour. PF-polygonal ferrite, AF-acicular ferrite, B-bainite and P-pearlite.

Figure 9.13 Effect of the cooling rate on the yield strength of the reference alloy #6 after prior deformation of 33 % reduction in the austenite below the $T_{nr}$, cooling to 575 ºC at different cooling rates and simulation of the coiling at 575 ºC for 1 hour.

Figure 9.14 Effect of the cooling rate on the ultimate tensile strength of the reference alloy #6 after prior deformation of 33 % reduction in the austenite below the $T_{nr}$, cooling to 575 ºC at different cooling rates and simulation the coiling at 575 ºC for 1 hour.

Figure 9.15 Effect of the cooling rate on the YS/UTS ratio of the reference alloy #6 after prior deformation of 33 % reduction in the austenite below the $T_{nr}$, cooling to 575 ºC at different cooling rates and simulation the coiling at 575 ºC for 1 hour. PF-polygonal ferrite, AF-acicular ferrite and P-pearlite.

Figure 9.16 Relationship between the YS/UTS ratio (longitudinal specimens) and the measured volume fraction of acicular ferrite in the experimental alloys #1 to #5 after laboratory hot rolling with an 86% reduction in total and rapid cooling at a rate of 47 º$Cs^{-1}$.

**List of tables:**

Table 3.1 Reduction/pass of hot rolling

Table.4.1 Specification of line pipe steels of API[12]

Table 5.1 Typical chemical composition of the current 11 mm line pipe steel of Mittal Steel, (wt%)

Table 5.2 The parameters of the hot rolling process at Mittal Steel

Table 5.3 Design of chemical composition ranges of alloys that were investigated (in wt%)

Table 6.1 Chemical compositions of the experimental alloys, in wt.%

Table 6.2 The composition of the etchant solutions

Table 6.3 Temperatures and soaking time of the treatment for undissolved particles

Table 6.4 Calculation equilibrium Nb carbonitride solution temperature

Table 6.5 Testing parameters for $T_{nr}$ at strain ranging from 0.15 to 0.32

Table 6.6 Testing parameters for $T_{nr}$ at inter-pass times ranging from 4 to 50 seconds

Table 6.7 Testing parameters for $T_{nr}$ at strain rate ranging from 0.1 to 2.22 $s^{-1}$

Table 7.1 Measured volume fraction of particles on replicas with/without shadowing in alloy #6

Table 7.2 Undissolved particles: types and sizes after reheating treatments of alloy #6

Table 7.3 Intercept length austenite grain size, in µm, versus reheating temperature and soaking time of alloy #6

Table 7.4 The non-recrystallisation temperature and pass strains of alloy #6

Table 7.5 The non-recrystallisation temperature of alloy #6 as affected by different inter-pass times

Table 7.6 The non-recrystallisation temperature and strain rates of alloy #6

Table 7.7 The laboratory hot rolling parameters for alloy #1

Table 7.8 Measured results of volume fraction of acicular ferrite

Table 7.9 Mechanical properties of the experimental alloys

Table 7.10 Mechanical properties of samples #A124 of the Mo-free alloy #6 with no coiling and no prior deformation

Table 7.11 Mechanical properties of samples #AF3F of alloy #3 (with 0.09% Mo) and with no coiling and no prior deformation

Table 7.12 Mechanical properties of samples #A113 of the Mo-free alloy #6 with 60 min coiling at 600 ºC without prior deformation
Table 7.13 Mechanical properties of samples #B113 of alloy #6 with 60 min coiling at 575 ºC without prior deformation
Table 7.14 Mechanical properties of samples #TEN06 for the Mo-free alloy #6 with 60 min coiling at 575 ºC and a 33% prior reduction below the $T_{nr}$